JOURNAL OF GEOPHYSICAL RESEARCH: SPACE PHYSICS, VOL. 118, 1319–1330, doi:10.1002/jgra.50169, 2013

Thermospheric atomic oxygen density estimates using the EISCAT Svalbard Radar

H. Vickers,[1] M. J. Kosch,[2,5] E. Sutton,[3] Y. Ogawa,[4] and C. La Hoz[1]

Received 19 September 2012; revised 31 January 2013; accepted 31 January 2013; published 31 March 2013.

[1] Coupling between the ionized and neutral atmosphere through particle collisions allows an indirect study of the neutral atmosphere through measurements of ionospheric plasma parameters. We estimate the neutral density of the upper thermosphere above ~250 km with the European Incoherent Scatter Svalbard Radar (ESR) using the year-long operations of the International Polar Year from March 2007 to February 2008. The simplified momentum equation for atomic oxygen ions is used for field-aligned motion in the steady state, taking into account the opposing forces of plasma pressure gradients and gravity only. This restricts the technique to quiet geomagnetic periods, which applies to most of the International Polar Year during the recent very quiet solar minimum. The method works best in the height range ~300–400 km where our assumptions are satisfied. Differences between Mass Spectrometer and Incoherent Scatter and ESR estimates are found to vary with altitude, season, and magnetic disturbance, with the largest discrepancies during the winter months. A total of 9 out of 10 in situ passes by the CHAMP satellite above Svalbard at 350 km altitude agree with the ESR neutral density estimates to within the error bars of the measurements during quiet geomagnetic periods.

Citation: Vickers, H., M. J. Kosch, E. Sutton, Y. Ogawa, and C. La Hoz (2013), Thermospheric atomic oxygen density estimates using the EISCAT Svalbard Radar, *J. Geophys. Res. Space Physics*, *118*, 1319–1330, doi:10.1002/jgra.50169.

1. Introduction

[2] Forecasting of space weather effects on the Earth's atmosphere and studies of long-term climate change both rely on observations and modeling of upper-atmosphere properties. In situ measurements of satellite drag can provide an average global picture of the upper-atmosphere neutral density but at one altitude with low temporal and spatial resolution. On the other hand, ground-based instruments (e.g., radars) monitor the atmosphere at a fixed location with good altitude and temporal resolution. Incoherent scatter (IS) radars measure the ionospheric parameters, typically in the height range 90–600 km. Collisions couple the ionized and neutral gas, which allows neutral atmosphere properties to be indirectly inferred via the observed ionospheric parameters. It is this characteristic that forms the basis of this study. Here we present and verify a technique to infer thermospheric neutral density using the European Incoherent Scatter (EISCAT) Svalbard radar (ESR) data recorded during the International Polar Year (IPY). The ultimate goal is to understand the thermospheric response on three different time scales, i.e., geomagnetic storms of a few hours, the solar cycle of 11 years, plus seasonal and long-term trends of multiple decades associated with climate change. In addition, radar observations of the polar cap thermospheric density are relatively rare. It is not yet known how well the globally averaged satellite observations, mostly from low and middle latitudes reflect the upper thermospheric behavior in the polar cap.

[3] Global satellite drag measurements at middle and high latitudes have shown that large geomagnetic storms can result in dramatic enhancements of the atomic oxygen density of several hundred percent at altitudes near 400 km [*Sutton et al.*, 2005; *Zhou et al.*, 2009]. On occasions the enhancement can reach up to almost an order of magnitude [*Bruinsma et al.*, 2006; *Liu and Lühr*, 2005]. In addition, changes in thermospheric composition occur [e.g., *Fuller-Rowell et al.*, 1991; *Rishbeth*, 1991; *Burns et al.*, 1995; *Field and Rishbeth*, 1997], which arise from atmospheric upwelling driven by Joule heating at high latitudes that circulates and redistributes atmospheric constituents globally. These substantial changes take place on time scales that can range from a few hours [e.g., *Sutton et al.*, 2009] to a few days. The thermosphere may also experience highly efficient cooling in the recovery stage of storms [*Lei et al.*, 2011]. This can even lead to "overcooling", where poststorm densities have been observed to be up to 36% below the quiet-time densities, prior to a large geomagnetic storm.

[4] As well as short-term, storm-driven changes in the thermosphere, satellite studies at middle latitudes have shown that the global thermosphere is gradually contracting [*Keating et al.*, 2000; *Marcos et al.*, 2005; *Emmert et al.*,

[1]Institute for Physics and Technology, University of Tromsø, Norway.
[2]Department of Physics, Lancaster University, UK.
[3]Air Force Research Laboratory, Kirtland, AFB, USA.
[4]National Institute of Polar Research, Tokyo, Japan.
[5]School of Physics, University of KwaZulu-Natal, Durban, 4001, South Africa.

Corresponding author: H. Vickers, Institute for Physics and Technology, University of Tromsø, Norway. (hannah.vickers@uit.no)

2169-9380/13/10.1002/jgra.50169

2008]. The rate of decrease in density at 400 km has been estimated to range from 2% to 5% per decade at solar maximum and minimum, respectively [*Emmert et al*., 2004, 2008]. Modeling work places a slightly lower estimate on the thermospheric density decline of typically 1% to 2% per decade at 400 km [*Qian et al*., 2006]. The cause of this contraction is linked to the long-term increases in CO_2 concentration, which have resulted in warming of the troposphere. However, CO_2 acts as a highly effective radiative coolant in the middle and upper atmosphere [*Roble*, 1995]. It is believed that this cooling is at least partly responsible for the long-term contraction of the thermosphere [*Cnossen*, 2012, and references therein].

[5] The MSIS (Mass Spectrometer and Incoherent Scatter) empirical neutral atmosphere model [*Hedin*, 1983, 1987, 1991] is a large database of experimental measurements from satellite and IS radar observations, which includes data from the high-latitude EISCAT mainland radars in Norway but no data from the polar cap ESR. MSIS uses daily F10.7 and 3-hourly *Ap* indices to parameterize solar and geomagnetic activity. The statistical nature of MSIS dictates that accurate predictions hold only during quiet and steady state conditions. Several studies have shown that significant differences exist between in situ measurements and MSIS-modeled thermospheric mass densities during geomagnetic disturbances [e.g., *Bruinsma et al*., 2006; *Burke et al*., 2007; *Forbes et al*., 2005]. The severity of underestimation by MSIS can range from a factor 2 [e.g., *Sutton et al*., 2005] up to as much as 5 when expressed in terms of the enhancement above the prestorm densities [*Liu and Lühr*, 2005]. *Zhou et al*. [2009] addressed this issue by developing a method that used the dependence of the mass density changes on Joule heating power and Sym-H indices to correct the NRLMSISE-00 model [*Picone et al*., 2002] estimates during disturbed conditions. Through an example test of this method, *Zhou et al*. [2009] showed that the average deviation between CHAMP satellite measurements and the NRLMSISE-00 estimates could be reduced by a factor of 3 at 400 km during storm activity.

[6] The coupling between the neutral atmosphere and ionized gas through collisions allows incoherent scatter radar measurements to derive neutral atmosphere parameters. Ground-based radars typically estimate the ion (T_i) and electron (T_e) temperature, electron density (N_e), and ion velocity (V_i). Employing ground-based radars in conjunction with the ion energy balance equation to study ion-neutral coupling in the *F* region has been carried out rather thoroughly at middle latitudes to infer neutral temperature and density [e.g., *Bauer et al*., 1970; *Swartz and Nisbet*, 1971; *Burnside et al*., 1988; *Nicolls et al*., 2006] as well as at high latitudes [e.g., *Blelly et al*., 2010]. This approach shows varying levels of agreement between experimentally derived density and the density obtained from empirical neutral atmosphere models. Authors of such studies have often tended to express the two estimates in terms of a ratio, usually referred to as the Burnside factor, after *Burnside et al*. [1987]. This is the multiplying factor of the *Banks* [1966] formula for the O + -O collision cross-section needed to achieve agreement between the collision frequencies obtained from experimental data and model values. Implicit in this is that the ion-neutral collision frequency is directly related to neutral density.

[7] Another approach considers the use of the ion momentum equation to study ion-neutral coupling. *Winser et al*. [1988] combined high-latitude EISCAT IS and Fabry-Perot interferometer optical observations at 240 km and found that MSIS predicted the ion-neutral collision frequency ν_{in} to be a factor 2 to 3 greater than that indicated by experimental measurements. Using the same technique, [Anderson *et al*., 2012] showed very good agreement existed at 260 km altitude between the Alaskan Poker Flat Incoherent Scatter Radar observations and MSIS, provided the data were mapped back to zero geomagnetic activity using magnetometer data. *Kosch et al*. [2010] used *F* region artificial heating experiments at the EISCAT ionospheric heating facility [*Rietveld et al*., 1993] to study ion outflow. They reported ion-neutral collision frequency estimates a factor of 2 to 3 times greater than the MSIS-90 model prediction for 400–500 km altitude.

[8] An alternative technique has been demonstrated by *Mikhailov and Lilensten* [2004], whereby Chapman functions were fitted to hourly-averaged EISCAT IS electron density profiles. Ionospheric plasma parameters were combined with the continuity equation for oxygen ions to extract seven thermospheric parameters. Good agreement between their results and the MSIS-86 model estimates of the thermospheric parameters at 300 km was found under quiet geomagnetic conditions. However, the authors reported model values of a factor 2 larger than their results during disturbed conditions.

[9] European Incoherent Scatter radar data are routinely analyzed using the Grand Unified Incoherent Scatter Design and Analysis Package (GUISDAP) [*Lehtinen and Huuskonen*, 1996] to obtain estimates of the plasma parameters. We use the plasma parameters inferred from ESR data to estimate the ion-neutral collision frequency ν_{in} under quiet geomagnetic conditions ($Kp \leq 2$). For the upper thermosphere, which is dominated by atomic oxygen, ν_{in} can be used to directly infer neutral density. In this study, we follow the data analysis procedure outlined by *Kosch et al*. [2010], because their study showed that the ion-momentum equation could be used with EISCAT radar data in the thermosphere with a good temporal resolution of a few minutes. Importantly, their method is not dependent on Fabry-Perot interferometer observations to be effective, and therefore does not limit the time or altitude range over which it can be routinely used. In addition, we also employ the technique of [Anderson *et al*., 2012] whose procedure allows for the removal of geomagnetic activity effects by binning the radar data according to the level of magnetic field perturbation observed on the ground. However, both *Kosch et al*. [2010] and [Anderson *et al*., 2012] only presented results from case studies in the auroral zone. We extend the previous high-latitude case studies to a year-long study in the polar cap for the first time using the ESR data.

[10] By including the entire first year of the IPY data set, which was near-continuous between March 2007 and February 2008, seasonal variations can also be studied. Uniquely, the ESR's location in the polar cap means that the thermosphere is almost permanently in sunlight, including most of the winter season. Because ESR measurements are absent from the MSIS database, it is also not known how accurately MSIS describes the upper thermosphere within the polar cap. We use our results to compare with the MSIS

estimates and in situ verification is provided by the CHAMP satellite drag measurements.

[11] The work is presented as follows; in section 2 we present the theoretical framework for the technique, which forms the basis for the manipulation and analysis of the ESR data, which is outlined in section 3. In section 4 the results of the statistical study are described, and discussed in comparison with model and satellite measurements in section 5. We conclude in section 6 with a summary of the important results of this study, and outline future work and the uses of these results.

2. Theoretical Framework

[12] We begin with the 13-moment ion momentum balance equation [*Schunk*, 1975] to estimate the thermospheric ion-neutral collision frequency, which is directly linked to neutral density [*Schunk and Nagy*, 2000]. This is conducted using IS measurements and assuming atomic oxygen as the only constituent. We use a form of the equation simplified for field-aligned ion motion in the topside ionosphere at high latitudes. A full derivation and justification for the simplifying assumptions can be found in *Ogawa* [2002]. The terms that are neglected are: advection due to subsonic flow, the magnetic mirror force resulting from ion temperature anisotropy, the Lorentz force associated with cyclotron motion, the height differential of the stress tensor in the vertical direction, and the force contributed by chemical reactions. These assumptions have been shown to be reasonable for case study estimates of the ion-neutral collision frequency using the EISCAT UHF radar [cf. *Kosch et al.*, 2010] and at ESR [cf. *Ogawa*, 2002] in the topside ionosphere. By restricting our analysis to quiet geomagnetic conditions only, i.e., $Kp \leq 2$, Joule heating [*Kosch and Nielsen*, 1995] and heat flux of ions and electrons due to particle precipitation also become negligible [cf. *Hardy et al.*, 1985, 1989], allowing us to assume equal ion and neutral temperatures. Quiet geomagnetic conditions permit us to assume a steady state ion motion, so that the time derivative of the ion velocity is also ignored. Lastly, we neglect the neutral wind speed, because for quiet geomagnetic conditions at high latitudes the vertical neutral wind is generally small, typically $15\,\mathrm{ms}^{-1}$ [*Aruliah and Rees*, 1995]. Fabry Perot interferometer optical data are only available during nighttime cloud-free skies, which are infrequent at high latitudes thus making estimates of the vertical neutral wind and temperature infrequent.

[13] The reduced form of the momentum conservation equation, rearranged to solve for ion-neutral collision frequency (ν_{in}) is

$$\nu_{\mathrm{in}} = -\frac{1}{V_{i\|}}\left(g\sin I + \frac{k_B}{n_{e\|}m_i}\frac{\partial}{\partial z}\left\{n_{e\|}\left(T_{e\|}+T_{i\|}\right)\right\}\right) \qquad \left(s^{-1}\right) \quad (1)$$

[14] Here k_B is the Boltzmann constant, z is altitude, m_i is the mass of atomic oxygen, $n_{e\|}$, $T_{e\|}$, $T_{i\|}$, and $V_{i\|}$ are the electron density, electron temperature, ion temperature, and ion velocity, respectively, measured in the field-parallel direction. All terms obtained by IS measurement are a function of altitude. The first term on the right-hand side of equation (1) is the downward force due to gravity (g), corrected for magnetic inclination angle I over Longyearbyen and altitude. The second term on the right-hand side of equation (1) is the plasma pressure gradient force exerted by the electrons and ions, which acts upward in the topside ionosphere due to the declining electron density with altitude. This term also accounts for enhanced electron heat fluxes, which may result from changes in the solar zenith angle (small during any data integration) or from particle precipitation (assumed small for quiet geomagnetic conditions).

[15] In the upper thermosphere the neutral density n_n is expressed in terms of the ion-neutral collision frequency and the average ion-neutral temperature (T_{in}) [*Schunk and Nagy*, 2000]

$$n_n = \frac{\nu_{\mathrm{in}}}{3.67\times10^{-11}\sqrt{T_{\mathrm{in}}}\left(1-0.064\log_{10}T_{\mathrm{in}}\right)^2} \qquad \left(\mathrm{m}^{-3}\right) \quad (2)$$

[16] Because we assume no heat sources, $T_{in} = T_i$, which is inferred from the IS data. The validity of our assumptions is also limited in height range by several factors. First, we assume a single species atmosphere, i.e., atomic oxygen only. It is therefore important to consider altitudes above 250 km to ensure that this assumption is fulfilled, because MSIS suggests that the ratio of atomic oxygen to molecular nitrogen, the next dominant species in the upper thermosphere, is less than 2 for most of the IPY below 250 km. Below 200 km the contributions of additional ion species complicates the analysis of EISCAT data and the ion composition is not very well known. Also, the transition altitude at which additional ion species becomes significant can increase to between 250 to 300 km, when the neutral atmosphere is heated under very disturbed geomagnetic conditions [*Lathuillère and Kofman*, 2006 and references therein]. However, this should not affect our results as we consider quiet conditions only. Second, around the F region peak plasma density, the gradient terms in equation (1) approach zero. Lastly, at high altitudes our assumption of steady state, i.e., V_i = constant, may break down. Hence, our neutral density estimate is effectively limited to between ~250 and 500 km altitude where our assumptions are best satisfied.

3. Experimental Measurements

3.1. Instrumentation

[17] During the IPY, the ESR [*Wannberg et al.*, 1997] (78°09′N, 16°01′E) ran near-continuously from March 2007 to February 2008. A special pulse code (ipy_fixed42p) was used to give high radar efficiency for topside altitudes between 200 and 400 km, with a range resolution of 2.2–4.5 km. The altitude range over which ESR measurements are made using this experiment lies between approximately 75 and 470 km. Because the ion momentum equation was simplified for field-aligned ion motion (equation (1)), data were obtained from the field-aligned 42 m ESR antenna only. Raw ESR data were recorded at 6 s time intervals. These data were integrated to 5 min to reduce the measurement uncertainty and were analyzed conventionally using GUISDAP.

3.2. Data Processing and Analysis

[18] The IPY data set coincided with deep solar minimum conditions. Low geomagnetic activity corresponding to $Kp \leq 2$ was satisfied for a large proportion of the IPY data set. Figure 1 shows the Kp index for the IPY period with 3 h resolution. $Kp \leq 2$ intervals are indicated by the black bars

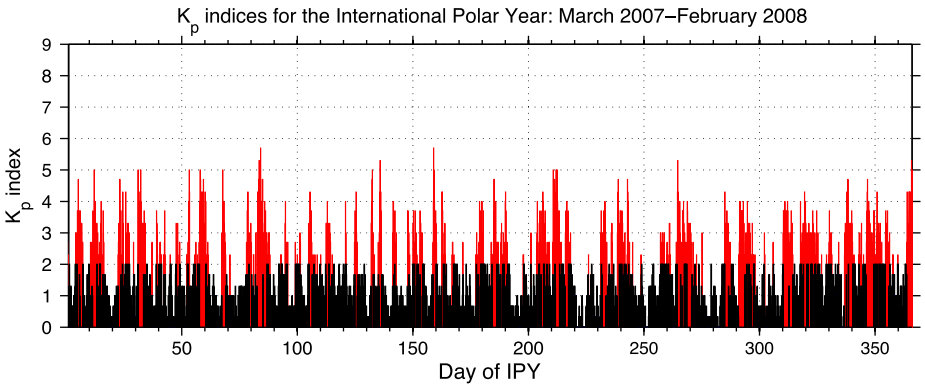

Figure 1. Geomagnetic activity throughout IPY; black bars for $Kp \leq 2$and red bars for $Kp > 2$.

and $Kp > 2$ intervals are highlighted by red bars. We note that the $Kp \leq 2$ intervals are evenly distributed throughout the IPY and were present for 70% of the time. We chose seven altitudes in the range 250 to 400 km at which to estimate the atomic oxygen density. These altitudes corresponded to 250, 285, 305, 325, 350, 370, and 390 km. For each range gate, which was closest to these fixed heights, the plasma-scale height $H = k_B(T_e + T_i)/m_i g$ was calculated. A data quality check was performed at each range gate and the adjacent gates above and below it. This was carried out by calculating the difference in electron density, which is expected from the ratio of the gate separation to the plasma-scale height at the range gate under consideration. The upper and lower bounds of the expected electron density difference was obtained from $e^{\pm \Delta h/H}$, where Δh is the height difference between adjacent range gates and H is the scale height at the range gate of interest. If the observed difference in electron densities between the center range gate and its adjacent gates fell outside the allowed upper and lower bounds, these data were rejected. Also, if the uncertainty in all four plasma parameters estimated by GUISDAP at any range gate exceeded 50% of the data value, the data point was rejected. Good data quality was required at all three range gates, i.e., the range gate which we use to estimate the neutral density at, and the gate above and below it, to calculate the plasma pressure gradient. Any 5 min profile containing a bad data point at any of these three range gates was rejected from further calculations. The filtering procedure selected 57% of all the available data at 250 km (33,460 data points) and 54% at 350 km (31,705 data points), with further reductions at altitudes above this due to declining signal-to-noise ratio (SNR) of the radar measurements.

[19] For the selected good-quality data, we calculated the plasma pressures given by $n_e k_B(T_e + T_i)$ at the three adjacent range gates. The range gate heights, typically spaced by 10 km, were interpolated onto a regular grid of 0.5 km spacing. This was necessary to estimate the pressure derivative at the original range gate altitude using a 5-point finite difference method, defined by the general expression

$$f'(z) = \frac{-f(z+2\Delta z) + 8f(z+\Delta z) - 8f(z-\Delta z) + f(z-2\Delta z)}{12\Delta z} \quad (3)$$

[20] Here z is the altitude at which the pressure derivative is desired, and the two interpolated pressure values above and below are located at $z \pm z$, $z \pm 2z$, with $\Delta z = 0.5$ km. This step size was deliberately chosen to be much smaller than the separation between adjacent range gates to ensure that any errors incurred in the approximation, proportional to Δz^4, would be small enough to ignore in calculations of the uncertainty in the neutral density estimates. An example height profile of the plasma pressure is shown in Figure 2, with the interpolated profile, which spans three range gates centered on the gate closest to 350 km shown by the pink-colored trace. The gravity term $g(z)$ of equation (1) was obtained for the inclination of the magnetic field above Longyearbyen ($I = 82°$) and adjusted for the altitude of the range gate, i.e., $g(z) = g0/(R_E + z)^2$ where $g0 = 9.81$ ms^{-2} is the gravitational acceleration at the Earth's surface and $R_E = 6370$ km is the Earth's radius. Because equation (1) depends inversely on the field-aligned ion velocity (V_i), neutral density estimates were not made using any IS data with zero ion velocity because this would lead to a nonfinite collision frequency estimate. Only absolute values of the ion-neutral collision frequency were used, because this could be positive or negative depending on the relative

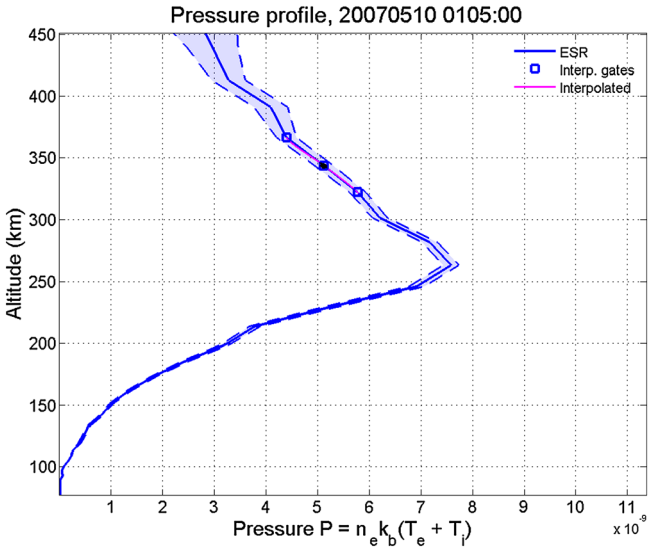

Figure 2. A typical profile of the plasma pressure in the upper thermosphere (blue) derived from ESR data, illustrating the interpolation across the three range gates (pink), which was used to obtain a numerical estimate of the pressure derivative.

magnitudes of the pressure and gravity terms and because V_i can be less or greater than zero for plasma motion toward or away from the radar respectively. A final check for data quality was done by accepting only the neutral density estimates, which were no greater than a factor of 5 smaller or greater than the median value over that hour in UT. This final process eliminated around 10% of the neutral density estimates made.

[21] The MSIS model estimate of the atomic oxygen density and its associated uncertainty was obtained using the Madrigal database application programming interface for the altitude, geographic coordinates, and time of the ESR data points. The application is documented on the web page, http://madrigal.haystack.mit.edu/madrigal/rt_matlab.html.

3.3. Geomagnetic Activity Binning

[22] Comparisons between the MSIS empirical model and the ESR data estimates made using equation (2) are most appropriate for minimal geomagnetic activity. We define this as zero perturbation in the geomagnetic field H-component. Because this is not a frequent occurrence, we extrapolate the statistical neutral density estimate as a function of ΔH back to $H = 0$. Magnetic field data for Longyearbyen were obtained from the Tromsø Geophysical Observatory. Technical problems associated with instrument movement due to changes in the permafrost made the Longyearbyen magnetometer data unreliable during the months of June and end of October/early November. This meant that our data set was reduced by the elimination of a further ~5000 neutral density estimates which had been made during these months. One-minute measurements of the declination (D), inclination (I), and total field (F) components from the magnetometer at Longyearbyen were used to obtain the H-component perturbations. This perturbation is related to the magnetic inclination (I) and total field (F) by the expression

$$\Delta H = \Delta F \cdot \cos I - \Delta I \cdot F \cdot \sin I \tag{4}$$

where the perturbation in inclination is ΔI and total field is ΔF with respect to their quiet mean values (3 per month). An average ΔH over consecutive 5 min intervals was calculated to synchronize the times with the ESR estimates. ESR data were sorted into 8 bins in ΔH whose absolute magnitude ranged from 0 to 40 nT in steps of 5 nT. This is the same procedure used by [Anderson *et al*., 2012] who found that for quiet geomagnetic conditions the number of cases where the absolute magnitude of ΔH (hereafter, $|\Delta H|$) exceeded 40 nT were too few to provide adequate statistics. Figure 3 shows the distribution of $|\Delta H|$ for the $Kp \leq 2$ intervals during the IPY. The chosen range of $|\Delta H|$ from 0 to 40 nT, accounts for 61% of the selected data.

[23] Both ESR and MSIS estimates of the neutral density were categorized in this way. ESR data were further divided into three subsets, each of four months to examine possible seasonal variations: March, April, October, and November for the spring and autumn equinoxes; May to August for the summer months; and November to February for the winter months. A linear fit was made using the median neutral density values in each $|\Delta H|$ bin

$$n_{\text{fit}} = C|\Delta H| + n0 \tag{5}$$

[24] The y-intercept ($n0$) gives the extrapolated "zero geomagnetic activity" for the ESR neutral density estimate. Only bins where the number of neutral density estimates

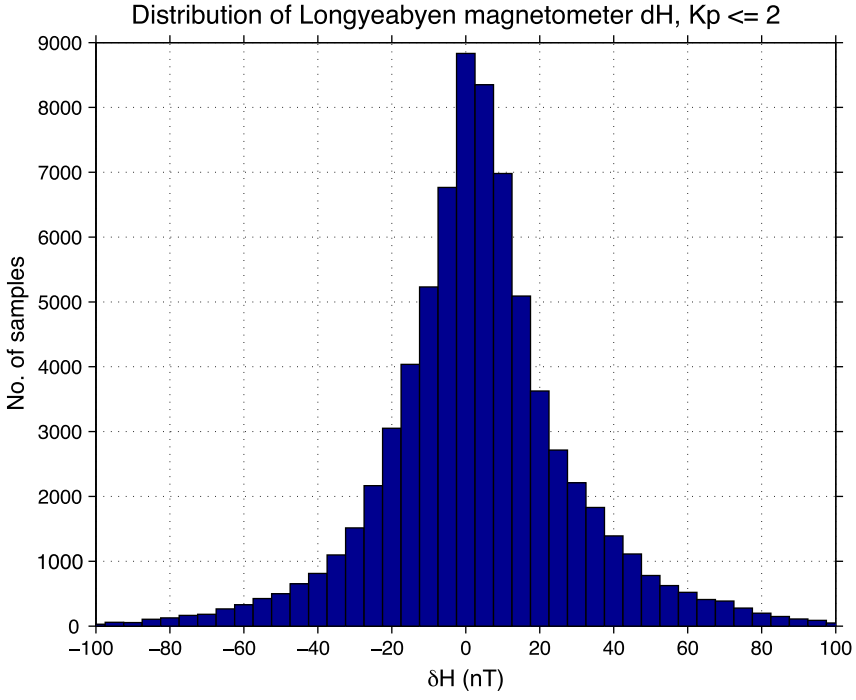

Figure 3. The distribution of Longyearbyen magnetometer H-component deflection over the IPY period for $Kp \leq 2$.

exceeded 20 were used to prevent large variances resulting from poor bin statistics.

[25] Our data processing allowed us to estimate the neutral density satisfactorily for each 5 min ESR profile before binning by geomagnetic activity. This provided statistical confidence without compromising on temporal resolution. In contrast, [Anderson *et al*., 2012] found it necessary to sacrifice temporal resolution to improve statistical confidence by performing the geomagnetic activity binning before making a final estimate of the ion-neutral collision frequency (and subsequently neutral density). They used the "zero activity" estimates for each plasma parameter to obtain a single estimate of the neutral density for their entire data set, which corresponded to several days of data.

3.4. CHAMP Satellite Measurements

[26] We use accelerometer measurements of satellite drag from the polar-orbiting low-altitude CHAMP satellite [*Reigber et al*., 2002] to provide estimates of the in situ total mass density. The CHAMP satellite was originally launched on 15 July 2000 into a high inclination orbit of 87.3° at an altitude of approximately 450 km. By 2007 however, the orbital altitude had decayed to close to 350 km. A set of CHAMP-ESR conjunctions during the IPY was found using the Satellite Situation Centre spacecraft locator tool (SSCWeb; http://sscweb.gsfc.nasa.gov/cgi-bin/Locator.cgi). We identified conjunctions as those data points when the CHAMP spacecraft coordinates passed within $\pm 1°$ of the ESR geographic latitude and longitude, i.e., 77.1–79.1°N and 15.0–17.0°E. Of the 37 CHAMP passes identified, 20 occurred during an interval of $Kp \leq 2$, and for 10 of these ESR estimates of the neutral density were also available. We excluded cases where $Kp > 2$ during the 3 h period prior to any CHAMP-ESR conjunction. This is important because the inertia of the thermosphere results in a time delay on the order of hours before it responds to changes in magnetospheric convection, such as those associated with geomagnetic disturbances [*Kosch et al*., 2001].

[27] The STAR accelerometer instrument on board CHAMP measures the sum of all the forces on the satellite surface. The reader is referred to *Sutton et al*. [2005] and *Sutton* [2009] where descriptions of the force model used in the STAR accelerometer data processing and estimations of the total mass density can be found. The time resolution of the CHAMP data used was 10 s, which corresponds to a spatial separation of approximately 80 km between consecutive measurements along the satellite track. We use the mass density measurements that have been normalized to 350 km with the MSIS model for the comparisons with the ESR results. These have been obtained by taking the actual CHAMP measurement at the satellite altitude and multiplying the measurement by the ratio of the MSIS mass density at 350 km to the MSIS mass density at the CHAMP altitude. For the IPY, the normalization should not result in a severe bias toward the MSIS estimate because the orbital altitude of CHAMP during this year was close to 350 km and well within the mass density scale height. For the purpose of the comparing both the ESR and CHAMP measurements, we have converted the CHAMP total mass density into an equivalent atomic oxygen number density.

4. Results

[28] This section is divided into two parts. In the first part, statistical averages of the neutral density estimates that are obtained from the geomagnetic data binning procedure are presented, and compared with MSIS. We concentrate on 250 and 350 km altitude, the former being associated with higher SNR and hence smaller measurement uncertainties, and the latter being the altitude closest to the CHAMP observations. The second part is dedicated to verifying our method using accelerometer data from the CHAMP spacecraft conjunctions.

4.1. Statistical Study

[29] Due to breaks in the operation of the ESR during both November and December 2007, the total number of 5 min winter samples (14,110) was approximately 1.5 times lower than the total number of samples for the summer (23,050) and equinox months (21,160). In total, after the data quality filtering procedures described in section 3 had taken place, the ESR IPY data set from the ipy_fixed42p experiment provided approximately 26,000 (250 km) and 23,500 (350 km) data points of 5 min temporal resolution with which to obtain neutral density estimates. The set of neutral density estimates was further reduced by approximately 20% through using only samples corresponding to $Kp \leq 2$ and another 10% reduction occurred through using $|\Delta H| \leq 40$ nT, bringing this total to approximately 18,000 and 16,000 estimates at 250 and 350 km, respectively.

[30] Figure 4 shows the ESR neutral density estimates at 250 km. Figures 4a, 4b, and 4c show equinox, summer and winter respectively, as defined in section 3.3. Red/blue data points correspond to the median $|\Delta H|$ bin values of the MSIS/ESR neutral density estimates respectively, with error bars representing the median fractional error in the neutral density over all samples in each $|\Delta H|$ bin. The linear fits made to the two data sets are indicated by the dashed lines. Figure 4d shows the relationship between $|\Delta H|$ and the median neutral density using all available IPY data. Figure 5 is in the same format as Figure 4 but for 350 km altitude. In each panel, the value of the y-intercept obtained from the linear fit is displayed for the ESR and MSIS data sets in the top left corner. This is the "zero geomagnetic activity" neutral density, which we use in comparing the ESR and MSIS estimates.

[31] The median MSIS neutral density at 250 km over all levels of geomagnetic activity is typically greater than the averaged ESR neutral density estimates by an amount depending on both season and $|\Delta H|$. The difference between the MSIS and ESR estimates ranges from $< 1 \times 10^{14}$ up to nearly 6×10^{14} m^{-3}, the greatest discrepancy over all $|\Delta H|$ bins being in the winter months (Figure 4c). Here the MSIS model densities are almost a factor 3 times greater than those inferred from the ESR measurements. The MSIS neutral density is higher in the winter months than in summer at 250 km, when both ESR and MSIS estimates are close in magnitude for all but the largest $|\Delta H|$ bins. For summer, the MSIS model is between 1 and 1.2 times the ESR values. At equinox, MSIS ranges from 1.1 to 1.5 times the ESR estimates, and in both cases the larger factor corresponds to the larger $|\Delta H|$ bins. It can also be seen that the ESR estimates show a weak decrease as the geomagnetic activity

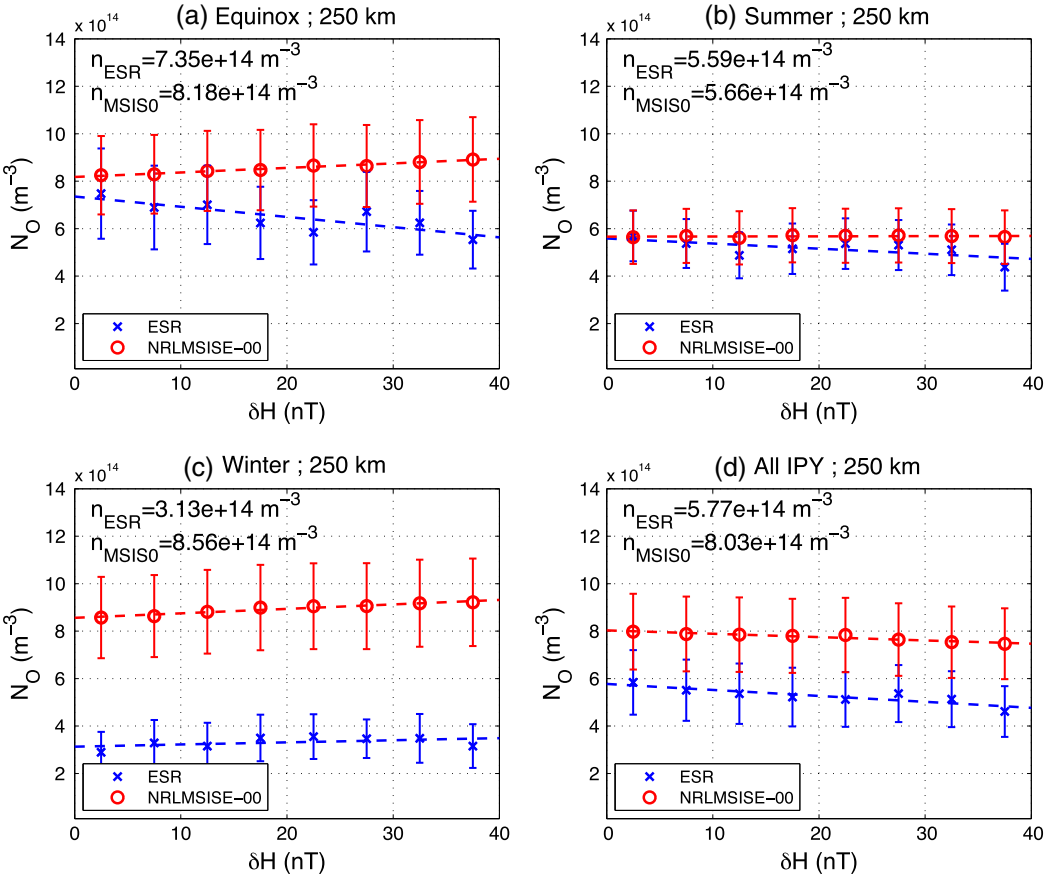

Figure 4. Neutral thermospheric density at 250 km altitude as a function of magnetometer *H*-component deflection for (a) equinox, (b) summer, (c) winter, and (d) all seasons. Red denotes the MSIS model and blue denotes the ESR estimate.

increases, while the MSIS densities show a weak increase. This magnitude of increase is however much smaller than the error associated with the bin values. The ESR estimates indicate that the neutral density is lowest in winter and greatest at equinox while MSIS indicates lowest densities in summer. For the full IPY data set at 250 km (Figure 4d), MSIS densities are typically higher than the ESR by 2 to 2.5 $\times$ 10^{14} m^{-3} across all $|\Delta H|$ bins. This is a factor of 1.3 to 1.5 times the ESR estimates.

[32] The ESR and MSIS results for 350 km, shown in Figure 5, agree with each other more closely over the majority of the $|\Delta H|$ bins compared to at 250 km. The seasonal dependence of the ESR-MSIS agreement at 350 km is much weaker compared to 250 km. A comparison of the derived zero-activity neutral density values from the ESR and MSIS data show that the ESR densities are 0.95, 0.89, and 1.01 times the MSIS zero-activity density for the equinox, summer, and winter months, respectively. Similarly to the summer results at 250 km, the difference between MSIS and ESR is consistently small over all $|\Delta H|$ bins for the summer months at 350 km. Figures 5a, 5b, and 5c also show that the error bars of the ESR and MSIS median bin densities overlap each other, indicating that the ratio of the two methods do not deviate far from unity for all seasons. In the case of the full IPY data set, the "zero activity" ESR neutral density estimate is 7.6 $\times$ 10^{13} m^{-3}, which is also in agreement with the MSIS density of 8.29 $\times$ 10^{13} m^{-3}, representing a discrepancy of only 9.1%. This is well within the ESR uncertainty of 28%.

[33] Figure 6a shows the height profile of the ESR to MSIS ratio $ESR_0/MSIS_0$ for the zero geomagnetic activity neutral density estimates obtained from using all IPY data (i.e., not season separated). The ratio is shown by the pink trace and the fractional error $\delta N/N$ by the blue trace. This error is estimated by propagating the errors in the ESR plasma parameters through the formulae used to obtain the ion-neutral collision frequency (equation (1)) and neutral density (equation (2)). The fractional error shown in Figure 6a is the median over all error estimates in the lowest activity bin ($0 < |\Delta H| \leq 5$ nT). While both profiles exhibit similarities in their behavior with altitude, the altitude where the errors minimize is at 250 km, whereas the best agreement between ESR and MSIS is attained at 350 km. At 250(350) km the ESR error is 0.26(0.28) and the ESR/MSIS ratio is 0.72(0.92). Thus, even though the error is smaller at 250 km than at 350 km the difference between the errors at 250 and 350 km is only 0.03 (i.e., 3%).

[34] Figure 6b shows the number of neutral density samples used in the averaging as a function of altitude. We show only the number of samples in the lowest magnetic activity bin, because this is the number of samples which contribute in the calculations of the averaged fractional error profile displayed in Figure 6a. Both the error profile in Figure 6a and the number of samples as a function of altitude follow

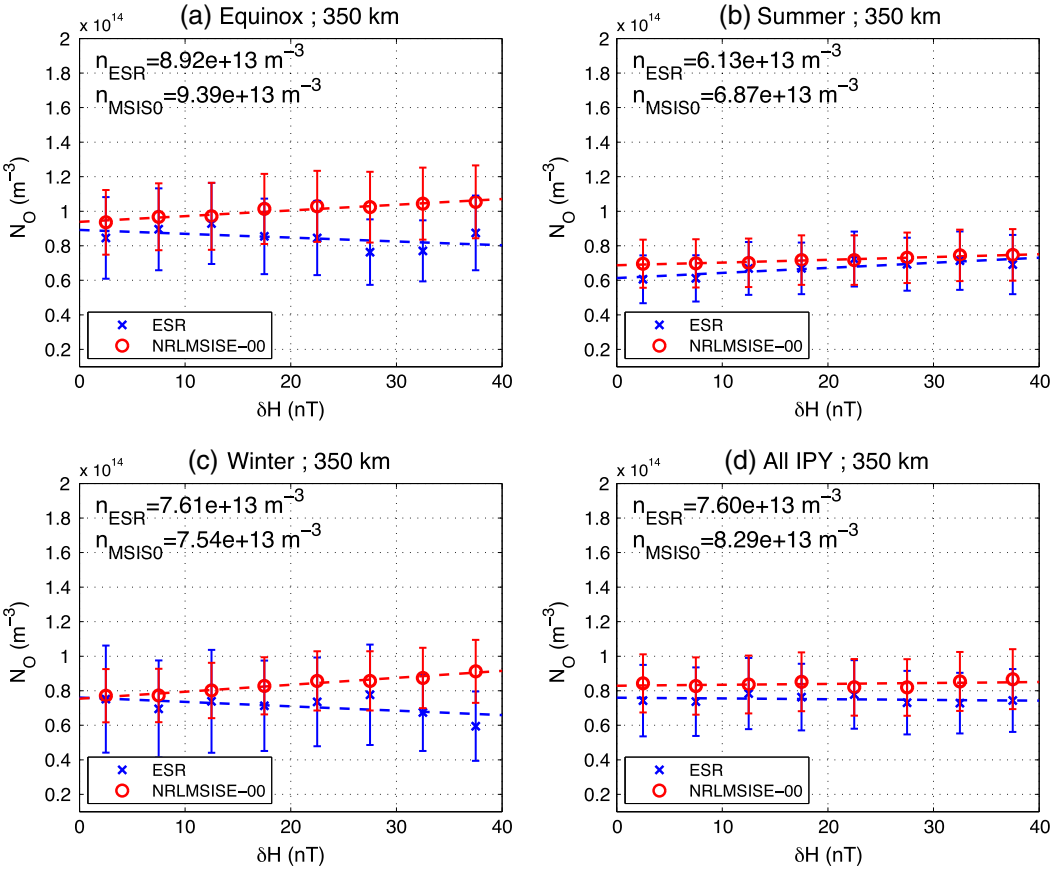

Figure 5. Same as Figure 4 but for 350 km altitude.

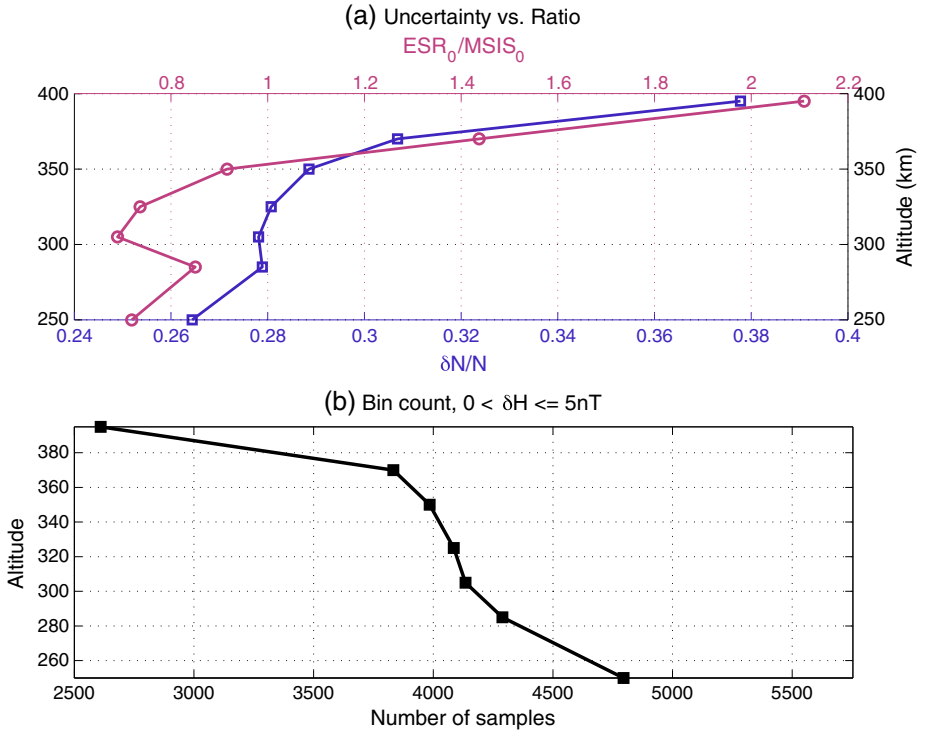

Figure 6. (a) Relative neutral density uncertainty with altitude (blue, lower axis) and the comparison with MSIS as a ratio (pink, upper axis) for zero geomagnetic activity. (b) Distribution of data samples for zero geomagnetic activity as a function of altitude.

Table 1. Summary of the CHAMP-ESR Comparisons. The Time and Location Is for Closest Approach to the ESR. The Average Number Density With Uncertainty Is Given for Both CHAMP and ESR as Well as the Percentage Difference Between Them and Their Ratio

Date (DOY)	UT	Lat.	Long.	CHAMP ($\times 10^{13}$ m^{-3})	ESR ($\times 10^{13}$ m^{-3})	$\frac{\lvert ESR-CHAMP\rvert}{ESR}$ (%)	$\frac{CHAMP}{ESR}$
1. 13/04/07 (103)	14:48	78.57	16.79	$9.73 \pm 6.6\%$	$11.85 \pm 41.6\%$	17.8	0.82
2. 03/05/07 (123)	02:51	78.59	16.79	$6.75 \pm 9.8\%$	$8.94 \pm 25.8\%$	24.5	0.76
3. 05/05/07 (125)	12:53	78.56	15.20	$10.93 \pm 6.7\%$	$13.78 \pm 41.7\%$	20.7	0.79
4. 15/06/07 (166)	22:43	77.43	16.70	$11.09 \pm 7.0\%$	$5.62 \pm 19.8\%$	97.4	1.97
5. 18/06/07 (169)	08:44	78.45	16.87	$7.89 \pm 8.4\%$	$9.81 \pm 34.0\%$	19.5	0.80
6. 28/06/07 (179)	21:38	77.51	15.09	$7.05 \pm 10.1\%$	$8.20 \pm 28.7\%$	14.0	0.86
7. 01/07/07 (182)	07:39	77.37	16.40	$8.29 \pm 8.0\%$	$9.61 \pm 32.4\%$	13.7	0.86
8. 12/08/07 (224)	17:27	77.12	15.32	$8.18 \pm 7.4\%$	$7.24 \pm 28.3\%$	12.9	1.13
9. 17/09/07 (260)	14:11	78.33	15.93	$7.15 \pm 7.9\%$	$7.76 \pm 25.4\%$	7.8	0.92
10. 30/09/07 (273)	12:54	77.86	16.70	$11.45 \pm 6.4\%$	$13.54 \pm 35.2\%$	15.4	0.85

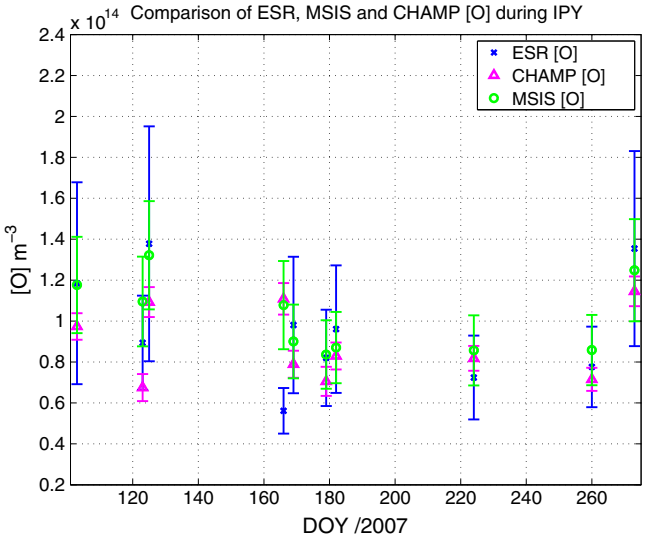

Figure 7. Neutral density at 350 km altitude derived from CHAMP satellite drag measurements (red) and the hour-averaged ESR estimates (blue) and the MSIS densities (green) for 10 conjunctions during the IPY where $Kp \leq 2$.

each other closely, which suggests strongly that the rapid increase in the errors above 350 km is associated with decreasing ESR sample size, and this is due to decreasing radar SNR with altitude.

4.2. CHAMP Results

[35] We present the first thermospheric neutral density comparisons from IS radar data and in situ spacecraft drag data within the polar cap. For this, all available ESR neutral density estimates at 350 km within the same hour of the CHAMP conjunction were used to obtain an averaged ESR density. Typically between 5 and 10 ESR samples were available to obtain the hour average. Table 1 shows the mean ESR neutral densities and their errors for the CHAMP passes where ESR data existed, and the results are shown in Figure 7.

[36] The difference between CHAMP and ESR neutral density estimates ranges from 8 to 24% with ESR consistently estimating a higher density than CHAMP in 8 out of 10 cases. This corresponds to a CHAMP-to-ESR density ratio ranging from 0.76 to 0.92 for these eight cases. In cases (4) and (8) the ESR estimate is below that of the CHAMP measurement, the CHAMP-to-ESR ratio being 1.97 and 1.13, respectively, for these cases. Figure 7 shows that in all but one case (4) the CHAMP measurement falls within the error bars of the ESR estimates. Where the CHAMP measurement is roughly two times greater than the ESR estimate (case 4), the uncertainty in the ESR estimate was in fact lowest out of all cases considered (~20%). The reasons for this discrepancy are not clear. We have also considered geomagnetic activity prior to the CHAMP pass [cf. *Aruliah et al.*, 1999], which can influence the thermospheric density [e.g., *Sutton et al.*, 2005; *Zhou et al.*, 2009] and composition [e.g., *Crowley et al.*, 2006]. While the $Kp \leq 2$ criterion was satisfied during and within the 3 h interval prior to the CHAMP pass, in both the cases where the ESR estimate was below that of the CHAMP measurement (cases 4 and 8), the *Kp* index had been raised to levels > 2 in the 24 h prior to the interval of the CHAMP measurement. These increased levels of activity had also been sustained for at least 12 h continuously during the 24 h period. In 7 of the 8 cases where the ESR estimate exceeded the CHAMP measurement and also fell within the uncertainty level of the estimate, the *Kp* index had remained below 2 during the 24 h preceding the CHAMP pass. The exception to this is case (10) where the ESR estimate exceeded CHAMP, but the *Kp* index had been continuously elevated to values ≥ 2 for more than 30 h before the interval we considered, excluding the 3 h interval prior to the CHAMP pass where we required $Kp \leq 2$.

5. Discussion

[37] This study has focused on the development of earlier methods that combine the ion momentum equation with incoherent scatter radar data in conjunction with magnetometer data to make estimates of the atomic oxygen density in the upper thermosphere. We have tested the method in a statistical sense by employing the unique IPY data set recorded by the ESR. Here we discuss the results which were presented in section 4 and some offer some explanations for similarities and discrepancies between our work and current literature.

[38] In section 4.1 it was shown that the MSIS model estimate for the neutral density varied from 1 to 1.5 times the ESR estimate during the equinox and summer months at 250 km, but could be as much as a factor 3 times the ESR density for the winter months. Earlier studies have found the MSIS model densities to exceed ion momentum equation based IS radar estimates by a factor ranging from

1.2 at 300 km under quiet geomagnetic conditions [*Mikhailov and Lilensten*, 2004] up to a factor 2 to 3 at altitudes of 240 km [e.g., *Winser et al*., 1988], which is consistent with our results.

[39] Figures 4 and 5 indicate differences in neutral density at 250 and 350 km between the equinox, summer, and winter seasons. It is well known from studies based on satellite drag measurements that the upper thermospheric density exhibits annual and semiannual variations. The thermospheric density is at a maximum during the equinox months with a primary minimum in July and secondary minimum in January [e.g., *Paetzold and Zschörner*, 1961; *Qian et al*. 2009; *Lei et al*., 2012b], and the amplitude difference between maximum and minimum can depend on both height and solar EUV flux [*Bowman et al*. 2008]. Although we do not endeavor to discuss the mechanisms for the seasonal variations, we note that our results for 350 km show that the density is indeed maximum in the equinox months (8.92×10^{13} m^{-3}), and lowest in summer (6.13×10^{13} m^{-3}) with the secondary minimum in winter (7.61×10^{13} m^{-3}). This is consistent with the expected pattern. However, while the density at 250 km is also greatest at equinox (7.35×10^{14} m^{-3}), our results indicate a minimum in the winter months (3.13×10^{14} m^{-3}) and a secondary minimum in summer (5.59×10^{14} m^{-3}). We anticipate that investigation of the solar activity dependence of the seasonal variation amplitude will be carried out in separate studies.

[40] The lack of agreement between MSIS and the ESR estimates at 250 km (see Figure 4) could have several reasons. At altitudes near the *F* region peak, which was typically 230 km during the IPY at ESR [*Zhang et al*., 2010], the pressure gradient approaches zero making its numerical estimation prone to significant uncertainty. The ion-neutral collision frequency is inversely proportional to ion velocity, which is generally small at the *F* region peak [e.g., *Wahlund et al*., 1992]. These factors increase the uncertainty of the ion-neutral collision frequency estimate. An additional factor is that MSIS does not incorporate ESR data and no other polar cap IS radar data are available, so MSIS is not necessarily reliable in this region.

[41] We found that the error associated with the ESR neutral density estimates was smaller at 250 km than at 350 km, even though the agreement between MSIS and ESR was in fact better and consistent across the seasons at an altitude of 350 km. However, we note that the difference between the fractional errors at 250 km and 350 km is only of the order 0.03 (i.e., 3%), a variation of ~10% and as such the errors are virtually equal. This result therefore agrees with the study of *Ogawa* [2002] who showed that ESR estimates of the ion-neutral collision frequency converged toward those from the MSIS-90 model at an altitude where the uncertainty in the collision frequency estimate minimized. *Ogawa* [2002] found best agreement in the range 400–500 km between estimates obtained from MSIS and ESR data. Their study was made using data recorded during solar maximum conditions when the atmosphere is expanded relative to solar minimum and so is consistent with our result.

[42] For the comparison between measurements made by the CHAMP satellite and the ESR data, 10 examples were identified where the satellite passed within $\pm 1^\circ$ of the ESR geographic coordinates and this was presented in section 4.2. It was found that in 8 of the 10 examples, the ESR estimates exceeded the CHAMP measurements. For the two conjunctions where the ESR estimates fell below the in situ measurements (cases 4 and 8 in Table 1), it is possible that the CHAMP satellite simply sampled localized regions of higher density, which were outside of the ESR beam. However, we note that higher geomagnetic activity preceded the interval when these two ESR-CHAMP conjunctions occurred. This may be simply a coincidence, but it is possible that the history of geomagnetic activity could determine how well the neutral density can be estimated using IS radar, because it is known that substantial and prolonged changes in the composition and density of the upper thermosphere can take place as a result of geomagnetic storms [e.g., *Fuller-Rowell et al*., 1991; *Burns et al*., 1995; *Liu and Lühr*, 2005; *Sutton et al*., 2005; *Bruinsma et al*., 2006]. The cases where lower ESR values were obtained after periods of higher geomagnetic activity may be an indicator of the "overcooling" effects [*Lei et al*., 2012a], which have been found to follow strong geomagnetic disturbances. The dependence of the ESR neutral density estimates on the time history of geomagnetic activity will be reported elsewhere.

[43] Comparisons between the MSIS-90 model and CHAMP measurements have been carried out by *Liu and Lühr* [2005]. For Northern Hemisphere cusp latitudes, they reported that MSIS densities were below those observed by CHAMP by typically 20 to 30% at 400 km. This was based on a data set from quiet, solar maximum conditions in 2002 with the difference calculated from $\log_e$(CHAMP/MSIS - 90). Because we have found good agreement between the MSIS and ESR estimates for 350 km, we might expect that ESR estimates should be approximately equivalent to MSIS in the MSIS-CHAMP comparison of *Liu and Lühr* [2005]. Our calculations of $\log_e$(CHAMP/ESR) using the data in Table 1 for 350 km give results that are in the opposite sense, i.e., the CHAMP observations lie between 8 to 28% below the ESR-inferred estimates. The exceptions are cases (4) and (8) where the CHAMP measurement was 68% and 12% greater, respectively. However, it is difficult to compare our results directly to *Liu and Lühr* [2005] because of the differences in altitude and solar activity.

6. Conclusion

[44] Ion-neutral coupling has allowed an indirect study of the neutral atmosphere through measurements of ionospheric plasma parameters. We have developed and presented a technique to estimate the upper thermosphere density above the ESR at altitudes above ~250 km by using the near-continuous first year of operations of the IPY from March 2007 to February 2008. This work represents an important addition to ground-based studies of the polar cap thermosphere, which is currently under-represented in the literature. The study is verified by, and complements the large database of global in situ measurements made by satellites. The method builds on earlier studies by using a simplified form of the ion momentum equation for atomic oxygen ions and considering steady state field-aligned motion only, taking into account the opposing forces of plasma pressure gradient and gravity. This restricts the technique to quiet geomagnetic periods ($Kp \leq 2$), which applies to most of the IPY during the recent very quiet solar minimum.

[45] At 250 km, which was close to the *F*-layer peak during the IPY, the ESR estimates of the atomic oxygen density are typically in the range 1 to 1.5 times smaller than the MSIS model when averaged over the IPY period. Differences between MSIS and ESR estimates are found to depend on both season and magnetic disturbance, with largest discrepancies during the winter months. Good agreement with the MSIS model is achieved without evidence of seasonal dependence at 350 km. This altitude was close to the orbital altitude of the CHAMP satellite during the IPY, allowing a comparison of in situ measurements and radar estimates of the neutral density. A total of 10 in situ passes by the CHAMP satellite above Svalbard show that the ESR neutral density estimates fall within the error bars of the satellite measurements for nine cases and exceed the CHAMP densities typically by 10 to 25%. The exception to this result coincides with periods of enhanced geomagnetic disturbances preceding the quiet interval ($Kp \leq 2$) when the measurements were made.

[46] We find that our method works best in the height range ~300–400 km where our assumptions are satisfied, at least for solar minimum. Because IS radar estimates of thermospheric neutral density appear to be reliable, the work presented here will be extended to solar maximum, to study the effect of geomagnetic activity and to determine the long-term trends in thermospheric neutral density.

[47] **Acknowledgments**. EISCAT is an international association supported by research organizations in China (CRIRP), Finland (SA), Germany (DFG, until end of 2011), Japan (NIPR and STEL), Norway (NFR), Sweden (VR) and the United Kingdom (NERC). We are grateful to Truls Hansen and Magnar Johnsen at Tromsø Geophysical Observatory for help with accessing and acquisition of magnetometer data used in this study, and to Bill Rideout at MIT Haystack Observatory for providing Madrigal database support.

References

Aruliah, A. L., and D. Rees (1995), The trouble with thermospheric vertical winds: geomagnetic, seasonal and solar cycle dependence at high latitudes, *J. Atmos. Sol. Terr. Phys.*, *57*, 597–609.

Aruliah, A. L., I. C. F. Muller-Wodarg, and J. Schoendorf (1999), Consequences of geomagnetic history on the high-latitude thermosphere and ionosphere: Averages, *J. Geophys. Res.*, *104*, 28073–28088.

Banks, P. (1966), Collision frequencies and energy transfer: Ions, *Planet. Space Sci.*, *14*(11), 1105–1122.

Bauer, P., P. Waldteufel, and D. Alcayde (1970), Diurnal variations of the atomic oxygen density and temperature determined from incoherent scatter measurements in the ionospheric F regions, *J. Geophys. Res.*, *75* (25), 4825–4832.

Blelly, P.-L., D. Alcaydé, and A. P. van Eyken (2010), A new analysis method for determining polar ionosphere and upper atmosphere characteristics from ESR data: Illustration with IPY period, *J. Geophys. Res.*, *115*, A09322, doi:10.1029/2009JA014876.

Bowman, B. R., W. K. Tobiska, and M. J. Kendra (2008), The thermospheric semiannual density response to solar EUV heating, *J. Atmos. Sol. Terr. Phys.*, *70*(11–12), 1482–1496, doi:10.1016/j.jastp.2008.04.020.

Bruinsma, S., J. M. Forbes, R. S. Nerem, and X. Zhang (2006), Thermosphere density response to the 20–21 November 2003 solar and geomagnetic storm from CHAMP and GRACE accelerometer data, *J. Geophys. Res. 111*, A06303, doi:10.1029/2005JA011284.

Burke, W. J., C. Y. Huang, F. A. Marcos, and J. O. Wise (2007), Interplanetary control of thermospheric densities during large magnetic storms, *J. Atmos. Sol. Terr. Phys.*, *69*, 279–287, doi:10.1016/j.jastp.2006.05.027.

Burns, A. G., T. L. Killeen, G. R. Carignan, and R. G. Roble (1995), Large Enhancements in the O/N_2 Ratio in the Evening Sector of the Winter Hemisphere During Geomagnetic Storms, *J. Geophys. Res.*, *100*(A8), 14,661–14,671, doi:10.1029/94JA03235.

Burnside, R. G., C. A. Tepley, and V. B. Wickwar (1987), The O^+-O collision cross section: Can it be inferred from aeronomical measurements?, *Ann. Geophys.*, *5*(6), 343–350.

Burnside, R. G., M. P. Sulzer, and J. Walker (1988), Determination of thermospheric temperatures and neutral densities at Arecibo from the ion energy balance, *J. Geophys. Res.*, *93*(A8), 8642–8650.

Cnossen, I. (2012), Climate Change in the Upper Atmosphere, in *Greenhouse Gases - Emission, Measurement and Management*, edited by G. Liu, InTech, 23 ISBN: 978-953-51-0323-3.

Crowley, G., et al. (2006), Global thermosphere-ionosphere response to onset of 20 November 2003 magnetic storm, *J. Geophys. Res.*, 111, A10S18, doi:10.1029/2005JA011518.

Emmert, J. T., J. M. Picone, J. L. Lean, and S. H. Knowles (2004), Global change in the thermosphere: Compelling evidence of a secular decrease in density, *J. Geophys. Res.*, *109*, A02301, doi:10.1029/2003JA010176.

Emmert, J. T., J. M. Picone, and R. R. Meier (2008), Thermospheric global average density trends, 1967–2007, derived from orbits of 5000 near-Earth objects, *Geophys. Res. Lett.*, *35*, L05101, doi:10.1029/2007GL032809.

Field, P. R., and Rishbeth H. (1997), The response of the ionospheric F2-layer to geomagnetic activity: an analysis of worldwide data, *J. Atmos. Sol. Terr. Phys.*, *59*, 163–180.

Forbes, J. M., G. Lu, S. Bruinsma, S. Nerem, and X. Zhang (2005), Thermosphere density variations due to the 15–24 April 2002 solar events from CHAMP/STAR accelerometer measurements, *J. Geophys. Res.*, *101*, A12S27, doi:10.1029/2004JA010856.

Fuller-Rowell, T. J., D. Rees, H. Rishbeth, A. G. Burns, T. L. Killeen, and R. G. Roble (1991), Modeling of composition changes during *F-region* storms: A reassessment, *J. Atmos. Terr. Phys.*, *53*, 541–550.

Hardy, D. A., M. S. Gussenhoven, and E. Holeman (1985), A statistical model of auroral electron precipitation, *J. Geophys. Res.*, *90*, 4229–4248.

Hardy, D. A., M. M. Gussenhoven, and D. Brautigam (1989), A statistical model of auroral ion precipitation, *J. Geophys. Res.*, *94*, 370–392.

Hedin, A. E. (1983), A revised thermospheric model based on mass spectrometer and incoherent scatter data: MSIS-83, *J. Geophys. Res.*, *88*, 10,170–10,188.

Hedin, A. E. (1987), MSIS-86 thermospheric model, *J. Geophys. Res.*, *92*, 4649–4662.

Hedin, A. E. (1991), Extension of the MSIS thermosphere model into the middle and lower atmosphere, *J. Geophys. Res.*, *96*(A2), 1159–1172.

Keating, G. M., R. H. Tolson, and M. S. Bradford (2000), Evidence of long term global decline in the Earth's thermospheric densities apparently related to anthropogenic effects, *Geophys. Res. Lett.*, *27*, 1523–1526.

Kosch, M. J., and E. Nielsen (1995), Coherent Radar Estimates of Average High-Latitude Ionospheric Joule Heating, *J. Geophys. Res.*, *100*(A7), 12,201–12,215.

Kosch, M. J., K. Cierpka, M. T. Rietveld, T. Hagfors, and K. Schlegel (2001), High-latitude ground-based observations of the thermospheric ion-drag time constant, *Geophys. Res. Lett.*, *28*(7), 1395–1398, doi:10.1029/2000GL012380.

Kosch, M. J., Y. Ogawa, M. T. Rietveld, S. Nozawa, and R. Fujii (2010), An analysis of pump-induced artificial ionospheric ion upwelling at EISCAT, *J. Geophys. Res.*, *115*, A12317, doi:10.1029/2010JA015854.

Lathuillère, C., and W. Kofman (2006), A short review on the F1-region ion composition in the auroral and polar ionosphere, *Adv. Space Res.*, *37*, 913–918.

Lehtinen, M. S., and A. Huuskonen (1996), General incoherent scatter analysis and GUISDAP, *J. Atmos. Terr. Phys.*, *58*, 435–452, doi:10.1016/0021-9169(95)00047-X.

Lei, J., J. P. Thayer, G. Lu, A. G. Burns, W. Wang, E. K. Sutton, and B. A. Emery (2011), Rapid recovery of thermosphere density during the October 2003 geomagnetic storms, *J. Geophys. Res.*, *116*, A03306, doi:10.1029/2010JA016164.

Lei, J., A. G. Burns, J. P. Thayer, W. Wang, M. G. Mlynczak, L. A. Hunt, X. Dou, and E. Sutton (2012a), Overcooling in the upper thermosphere during the recovery phase of the 2003 October storms, *J. Geophys. Res.*, *117*, A03314, doi:10.1029/2011JA016994.

Lei, J., T. Matsuo, X. Dou, E. Sutton, and X. Luan (2012b), Annual and semiannual variations of thermospheric density: EOF analysis of CHAMP and GRACE data, *J. Geophys. Res.*, *117*, A01310, doi:10.1029/2011JA017324.

Liu, H., and H. Lühr (2005), Strong disturbance of the upper thermospheric density due to magnetic storms: CHAMP observations, *J. Geophys. Res.*, *110*, A09S29, doi:10.1029/2004JA010908.

Marcos, F. A., J. O. Wise, M. J. Kendra, N. J. Grossbard, and B. R. Bowman (2005), Detection of a long-term decrease in thermospheric neutral density, *Geophys. Res. Lett.*, *32*, L04103, doi:10.1029/2004GL021269.

Mikhailov, A. V., and J. Lilensten (2004), A Revised Method to Extract Thermospheric Parameters from Incoherent Scatter Observations, *Annals of Geophysics*, *47*, 985–1008.

Nicolls, M. J., N. Aponte, S. A. Gonza´lez, M. P. Sulzer, and W. L. Oliver (2006), Daytime F region ion energy balance at Arecibo for moderate to high solar flux conditions, *J. Geophys. Res.*, *111*, A10307, doi:10.1029/2006JA011664.

Ogawa, Y. (2002), Generation Mechanisms of Ion Upflow in the Polar Topside Ionosphere, Ph.D. thesis, STEL, Nagoya University, Japan.

Paetzold, H. K., and H. Zschörner (1961), An annual and a semiannual variation of the upper air density, *Pure Appl. Geophys.*, *48*, 85–92, doi:10.1007/BF01992371.

Picone, J. M., A. E. Hedin, D. P. Drob, and A. C. Aikin (2002), NRLMSISE-00 empirical model of the atmosphere: Statistical comparisons and scientific issues, *J. Geophys. Res.*, *107*(A12), 1468, doi:10.1029/2002JA009430.

Qian, L., R. G. Roble, S. C. Solomon, and T. J. Kane (2006), Calculated and observed climate change in the thermosphere, and a prediction for solar cycle 24, *Geophys. Res. Lett.*, *33*, L23705, doi:10.1029/2006GL027185.

Qian, L., S. C. Solomon, and T. J. Kane (2009), Seasonal variation of thermospheric density and composition, *J. Geophys. Res.*, *114*, A01312, doi:10.1029/2008JA013643.

Reigber, C., H. Lühr, and P. Schwintzer (2002), CHAMP mission status, *Adv. Space Res.*, *30*, 129–134.

Rietveld, M. T., H. Kohl, H. Kopka, and P. Stubbe (1993), Introduction to ionospheric heating at Tromsø - 1. Experimental overview, *J. Atmos. Terr. Phys.*, *55*, 577–599.

Rishbeth, H. (1991), F-region storms and thermospheric dynamics, *J. Geomag. Geoelectr.*, *43*, 513–524.

Roble, R. G. (1995), Energetics of the mesosphere and thermosphere, in *The Upper Mesosphere and Lower Thermosphere: A Review of Experiment and Theory*, Geophys. Monogr. Ser., 87, edited by R. M. Johnson, and T. L. Killeen, pp. 1–21, AGU, Washington, D. C.

Schunk, R. W. (1975), Transport equations for aeronomy, *Planet. Space Sci.*, *23*, 437–485.

Schunk, R. W., and A. F. Nagy (2000), *Ionospheres: Physics, Plasma Physics, and Chemistry*, 270 pp. Cambridge Univ. Press, New York.

Sutton, E. K., J. M. Forbes, and R. S. Nerem (2005), Global thermospheric neutral density and wind response to the severe 2003 geomagnetic storms from CHAMP accelerometer data, *J. Geophys. Res.*, *110*, A09S40, doi:10.1029/2004JA010985.

Sutton, E. K. (2009), Normalized force coefficients for satellites with elongated shapes, *J. Spacecraft and Rockets*, *46*(1), 112–116, doi:10.2514/1.40940.

Sutton, E. K., Forbes, J. M., and D. J. Knipp (2009), Rapid response of the thermosphere to variations in Joule heating, *J. Geophys. Res.*, *114*, A04319, doi:10.1029/2008JA013667.

Swartz, W. E., and J. S. Nisbet (1971), Diurnal variation of the neutral temperature profile at Arecibo from incoherent scatter measurements and its relevance to the 1400-hour density maximum, *J. Geophys. Res.*, *76*(1), 185–196.

Wahlund, J. -E., H. J. Opgenoorth, I. Häggström, K. J. Winser, and G. O. L. Jones (1992), EISCAT observations of topside ionospheric ion outflows during auroral activity: Revisited, *J. Geophys. Res.*, *97* (A3), 3019–3037, doi:10.1029/91JA02438.

Wannberg, G., et al. (1997), The EISCAT Svalbard radar: A case study in modern incoherent scatter radar system design, *Radio Sci.*, *32*(6), 2283–2307, doi:10.1029/97RS01803.

Winser, K. J., A. D. Farmer, D. Rees, and A. Aruliah (1988), Ion-neutral dynamics in the high latitude ionosphere: First results from the INDI experiment, *J. Atmos. Terr. Phys.*, *50*, 369–377.

Zhang, S.-R., J. M. Holt, A. P. van Eyken, C. Heinselman, and M. McCready (2010), IPY observations of ionospheric yearly variations from high- to middle-latitude incoherent scatter radars, *J. Geophys. Res.*, *115*, A03303, doi:10.1029/2009JA014327.

Zhou, Y. L., S. Y. Ma, H. Lühr, C. Xiong, and C. Reigber (2009), An empirical relation to correct storm-time thermospheric mass density modeled by NRLMSISE-00 with CHAMP satellite air drag data, *Adv. Space Res.*, *43*, 819–828.